showed no mortality, with a modestly enhanced memory CD8 T cell differentiation and viral control (fig. S12). Taken together, these data are consistent with a model in which uncontrolled viral replication resulted in overstimulation of vaccine-elicited $T_H1$ CD4 cells, leading to generalized inflammation and multi-organ system failure (fig. S13).

Our data demonstrate that a vaccine that elicits primarily CD4 T cells can result in lethal immunopathology after challenge with a persistently replicating virus by a mechanism that involves hyperstimulation of vaccine-elicited CD4 T cells by uncontrolled viral replication. Both antiviral CD8 T cells and antibodies that limit viral replication abrogate this pathology. These data show that vaccine-elicited CD4 T cells can trigger immunopathology and mortality in certain settings.

Although the extent to which this phenomenon may occur in humans has not yet been determined, this mechanism is potentially generalizable to other vaccines that primarily induce CD4 T cells in the absence of other effective antiviral immune responses. A previous study reported that a vaccine that encoded an SIV CD4 T cell epitope led to higher viral loads and accelerated AIDS progression relative to controls after SIV challenge in rhesus monkeys (28), although SIV-specific CD4 T cell responses were not directly measured in that study. Moreover, because activated CD4 T cells also can serve directly as targets for HIV, vaccine-elicited CD4 T cells could theoretically have multifactorial negative effects (29). These findings warrant a thorough reevaluation of CD4 T cell responses, especially in the context of chronic infection.

## REFERENCES AND NOTES

1. J. C. Sun, M. J. Bevan, *Science* **300**, 339–342 (2003).
2. D. J. Shedlock, H. Shen, *Science* **300**, 337–339 (2003).
3. E. M. Janssen *et al.*, *Nature* **421**, 852–856 (2003).
4. E. M. Janssen *et al.*, *Nature* **434**, 88–93 (2005).
5. M. Matloubian, R. J. Concepcion, R. Ahmed, *J. Virol.* **68**, 8056–8063 (1994).
6. M. Battegay *et al.*, *J. Virol.* **68**, 4700–4704 (1994).
7. R. D. Cardin, J. W. Brooks, S. R. Sarawar, P. C. Doherty, *J. Exp. Med.* **184**, 863–871 (1996).
8. A. Grakoui *et al.*, *Science* **302**, 659–662 (2003).
9. R. D. Aubert *et al.*, *Proc. Natl. Acad. Sci. U.S.A.* **108**, 21182–21187 (2011).
10. M. Lichterfeld *et al.*, *J. Acquir. Immune Defic. Syndr.* **59**, 1–9 (2012).
11. R. R. Amara, P. Nigam, S. Sharma, J. Liu, V. Bostik, *J. Virol.* **78**, 3811–3816 (2004).
12. F. Rodriguez, S. Harkins, J. M. Redwine, J. M. de Pereda, J. L. Whitton, *J. Virol.* **75**, 10421–10430 (2001).
13. H. Streeck, M. P. D'Souza, D. R. Littman, S. Crotty, *Nat. Med.* **19**, 143–149 (2013).
14. M. A. Williams, E. V. Ravkov, M. J. Bevan, *Immunity* **28**, 533–545 (2008).
15. E. J. Wherry, J. N. Blattman, K. Murali-Krishna, R. van der Most, R. Ahmed, *J. Virol.* **77**, 4911–4927 (2003).
16. S. N. Waggoner, M. Cornberg, L. K. Selin, R. M. Welsh, *Nature* **481**, 394–398 (2012).
17. P. Penaloza-MacMaster *et al.*, *J. Exp. Med.* **211**, 1905–1918 (2014).
18. J. M. Kim, J. P. Rasmussen, A. Y. Rudensky, *Nat. Immunol.* **8**, 191–197 (2007).
19. M. Bruns, J. Cihak, G. Müller, F. Lehmann-Grube, *Virology* **130**, 247–251 (1983).
20. T. Dao *et al.*, *PLOS ONE* **4**, e6730 (2009).
21. C. Dow *et al.*, *J. Virol.* **82**, 11734–11741 (2008).
22. R. J. May *et al.*, *Clin. Cancer Res.* **13**, 4547–4555 (2007).
23. D. Ou, L. A. Mitchell, D. Décarie, S. Gillam, A. J. Tingle, *Virology* **235**, 286–292 (1997).
24. S. I. Abrams, S. F. Stanziale, S. D. Lunin, S. Zaremba, J. Schlom, *Eur. J. Immunol.* **26**, 435–443 (1996).
25. D. Homann *et al.*, *Virology* **363**, 113–123 (2007).
26. L. M. Fahey *et al.*, *J. Exp. Med.* **208**, 987–999 (2011).
27. A. Crawford *et al.*, *Immunity* **40**, 289–302 (2014).
28. S. I. Stapans *et al.*, *Proc. Natl. Acad. Sci. U.S.A.* **101**, 13026–13031 (2004).
29. A. S. Fauci, M. A. Marovich, C. W. Dieffenbach, E. Hunter, S. P. Buchbinder, *Science* **344**, 49–51 (2014).

## SUPERCONDUCTIVITY

# Charge ordering in the electron-doped superconductor Nd₂₋ₓCeₓCuO₄

Eduardo H. da Silva Neto,[1,2,3,4]*† Riccardo Comin,[1,2]* Feizhou He,[5] Ronny Sutarto,[5] Yeping Jiang,[6] Richard L. Greene,[6] George A. Sawatzky,[1,2] Andrea Damascelli[1,2]†

In cuprate high-temperature superconductors, an antiferromagnetic Mott insulating state can be destabilized toward unconventional superconductivity by either hole or electron doping. In hole-doped (p-type) cuprates, a charge ordering (CO) instability competes with superconductivity inside the pseudogap state. We report resonant x-ray scattering measurements that demonstrate the presence of charge ordering in the n-type cuprate Nd₂₋ₓCeₓCuO₄ near optimal doping. We find that the CO in Nd₂₋ₓCeₓCuO₄ occurs with similar periodicity, and along the same direction, as in p-type cuprates. However, in contrast to the latter, the CO onset in Nd₂₋ₓCeₓCuO₄ is higher than the pseudogap temperature, and is in the temperature range where antiferromagnetic fluctuations are first detected. Our discovery opens a parallel path to the study of CO and its relationship to antiferromagnetism and superconductivity.

Copper oxide superconductors are susceptible to a number of instabilities, but the relevance of these phases to the superconducting pairing mechanism is unclear. Charge ordering (CO) has emerged as a universal feature of hole-doped (p-type) cuprates, but it has so far not been detected in n-type cuprates (1) (Fig. 1A). Early evidence for a CO in the cuprates came from the detection in La-based cuprates of a periodic organization of spins and charge known as stripes (2–5), where the charge is periodic every four lattice constants along the Cu-O bond direction. More recently, following evidence for Fermi surface reconstruction from quantum oscillations (6, 7), nuclear magnetic resonance (8) and x-ray scattering measurements (9, 10) have directly shown the presence of a similar CO competing with superconductivity in Y-based cuprates. The opportunity to directly probe CO in reciprocal space has further propelled several resonant x-ray scattering measurements of the Y-based family (11–13) as well as the detection of CO in Bi cuprates (14–16)—substantiating earlier surface evidence by scanning tunneling microscopy (17–20)—and also in the single-layer Hg compound (21).

Studies of Bi-based cuprates, for which a considerable amount of angle-resolved photoemission spectroscopy (ARPES) data are available, show that the CO wave vector connects the ends of the Fermi arcs (14, 15)—an observation that links the existence of CO to the pseudogap in hole-doped systems. Additionally, doping-dependent measurements on bilayer systems (9, 13, 22, 23) find charge ordering to be most pronounced in a region of hole doping near $x = 1/8$, where stripes are predominant in La-based cuprates (2, 3). These results raise the questions of whether the

[1]Department of Physics and Astronomy, University of British Columbia, Vancouver, British Columbia V6T 1Z1, Canada. [2]Quantum Matter Institute, University of British Columbia, Vancouver, British Columbia V6T 1Z4, Canada. [3]Max Planck Institute for Solid State Research, D-70569 Stuttgart, Germany. [4]Quantum Materials Program, Canadian Institute for Advanced Research, Toronto, Ontario M5G 1Z8, Canada. [5]Canadian Light Source, Saskatoon, Saskatchewan S7N 2V3, Canada. [6]Center for Nanophysics and Advanced Materials and Department of Physics, University of Maryland, College Park, MD 20742, USA.
*These authors contributed equally to this work. †Corresponding author. E-mail: ehda@physics.ubc.ca (E.H.d.S.N.); damascelli@physics.ubc.ca (A.D.)
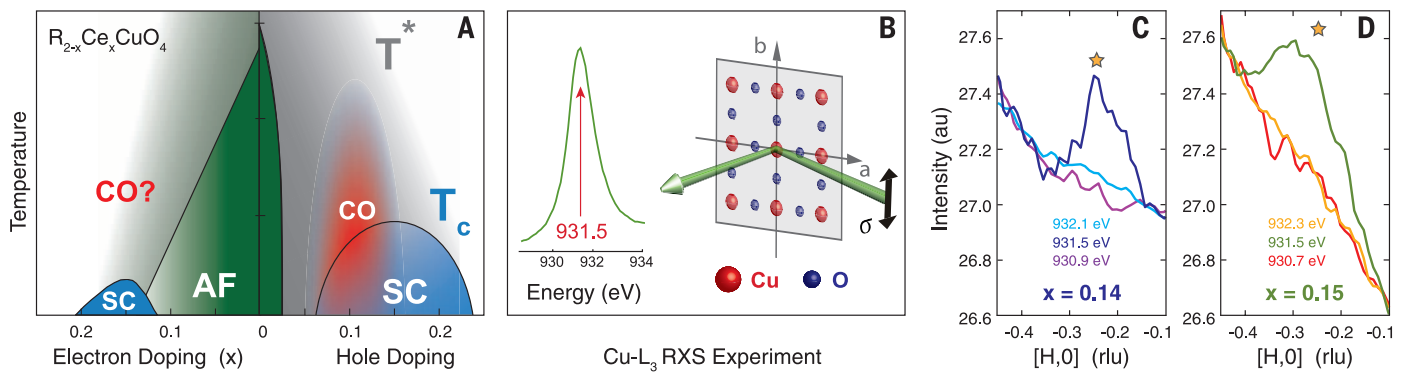
**Fig. 1. Charge ordering in electron-doped cuprates.** (**A**) Temperature-doping phase diagram for the cuprates, including the AF parent state (green), the superconductivity (SC, blue), and distinct n-type (faded green) and p-type (gray) pseudogap phases. The CO phase observed in p-type cuprates is marked in red. (**B**) The Cu-$L_3$ absorption edge at 931.5 eV ($2p \rightarrow 3d$ transition) and a schematic of the scattering geometry. (**C** and **D**) On- and off-resonance θ scans at 22 K, showing the RXS diffraction signal as a function of in-plane momentum transfer ($H$) along the Cu-O bond direction [see (B)] for $x = 0.14$ and $x = 0.15$, respectively. To provide a better comparison, the off-resonance scans were rescaled to match the tails of the on-resonance θ scans. The yellow stars mark the $H$ values of highest intensity for the two samples (obtained from Fig. 3).

particular phenomenology of the hole-doped cuprates such as the pseudogap-induced Fermi arcs, or the propensity toward stripe formation, are necessary ingredients for CO formation, or whether CO is a generic electronic property of the $CuO_2$ layer that is ubiquitous to all cuprates including n-type materials.

Here, we report resonant x-ray scattering (RXS) measurements on the electron-doped cuprate superconductor $Nd_{2-x}Ce_xCuO_4$ (*24*). Our studies were performed on samples with doping levels ($x = 0.14 \pm 0.01$ and $x = 0.15 \pm 0.01$) for which quantum oscillations indicate a small Fermi surface (*25*, *26*). We use the standard scattering geometry (Fig. 1B) (*24*), similar to previous studies (*9*, *14*, *15*). The tetragonal $b$ axis of the sample is positioned perpendicular to the scattering plane, allowing the in-plane components of momentum transfer to be accessed by rotating the sample around the $b$ axis (θ scan). For RXS measurements, the energy of the incoming photons is fixed to the maximum of the Cu-$L_3$ absorption edge, which is at $E \approx 931.5$ eV (Fig. 1B).

Our main finding is summarized in Fig. 1, C and D. An RXS peak is observed at an in-plane momentum transfer of $H \approx -0.24$ rlu (reciprocal lattice units) along the Cu-O bond direction; this is notably similar in periodicity and direction to the x-ray scattering peaks found in the hole-doped materials (*3*–*5*, *9*–*16*, *21*, *23*). The use of photons tuned to the Cu-$L_3$ edge is expected to greatly enhance the sensitivity in our measurement to charge modulations involving the valence electrons in the $CuO_2$ planes (*3*). As the photon energy is tuned away from resonance, the distinct peak near $H = -0.24$ disappears, thus confirming its electronic origin (Fig. 1, C and D) (*24*). This shows the presence of charge ordering in an electron-doped cuprate.

Further insights into charge ordering formation are obtained by temperature-dependent measurements. The distinct CO peak observed at low temperatures (Fig. 2, A and B) weakens as the temperature is raised, but disappears only above
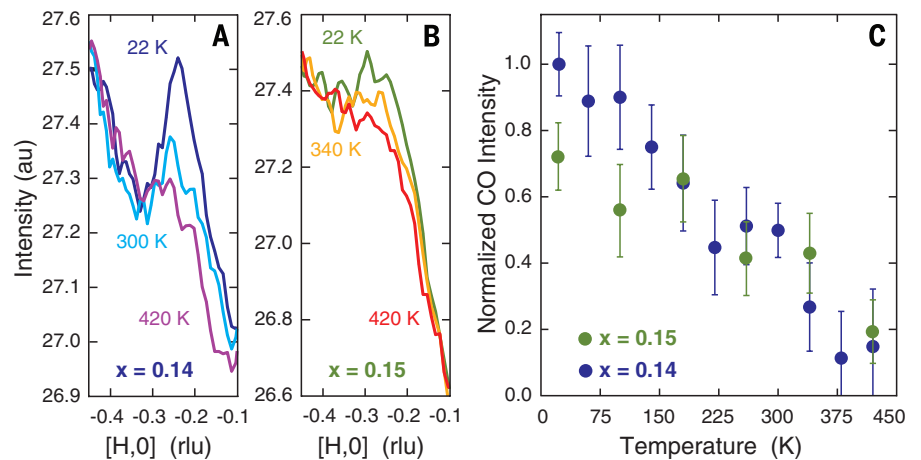


**Fig. 2. Temperature dependence of the CO.** (**A** and **B**) On-resonance θ scans for $x = 0.14$ and $x = 0.15$ samples, respectively, at select temperatures, showing that the onset of the charge ordering occurs above 300 K. (**C**) Temperature dependence of the RXS intensity for the two samples in (A) and (B) obtained from the maxima of the background-subtracted peaks. The intensity in (C) is normalized to the maximum value between the two samples; the error bars represent the standard errors from Lorentzian fits to the background-subtracted peaks (*24*).

300 K. Although a temperature evolution is clearly seen in the raw data (Fig. 2, A and B, and fig. S3), the small size of the peak relative to the high-temperature background precludes a precise determination of an onset temperature. Nonetheless, within the detection limits of the experiment, the CO seems to gradually develop with lowering of temperature starting around 340 K (Fig. 2C). Note that this temperature is much higher than the pseudogap onset in $Nd_{2-x}Ce_xCuO_4$ [~80 to 170 K in the $x = 0.14$ to 0.15 doping range (*1*, *27*, *28*)], in clear contrast to observations in hole-doped cuprates, where the p-type pseudogap either precedes or matches the emergence of CO (*9*–*15*, *21*–*23*). This dichotomy is not completely unexpected given that the pseudogaps observed in p- and n-type cuprates are dissimilar in many ways (*1*). In particular, the n-type pseudogap has been asso-

ciated with the buildup of antiferromagnetic (AF) correlations that first appear below 320 K (for $x = 0.145$ samples), as determined by inelastic neutron scattering measurements (*27*–*29*). Interestingly, the temperature evolution of the CO resembles the soft onset of AF correlations (*28*)—an observation that suggests a connection between CO and AF fluctuations in electron-doped cuprates.

We now use the available knowledge of the Fermi surface of $Nd_{2-x}Ce_xCuO_4$ to further investigate the connection between AF and CO formation. We find that the CO peak, although broad, is centered around an in-plane momentum transfer $Q_{CO} = 0.23 \pm 0.04$ and $Q_{CO} = 0.24 \pm 0.04$ for $x = 0.14$ and $x = 0.15$, respectively (Fig. 3, A and B). Comparison of $Q_{CO}$ to the Fermi surface topology measured by ARPES (Fig. 3C, left panel) shows that its value is consistent with scattering between

the parallel segments near $(\pi, 0)$. Thanks to the relative robustness of the AF phase in n-type cuprates, the Fermi surface has often been interpreted to undergo $(\pi, \pi)$ folding along the AF zone boundary—a scenario that is consistent with both ARPES (30) and quantum oscillation results (25). In this context, $Q_{CO}$ would connect opposite sides of electron pockets centered at $(\pi, 0)$ (Fig. 3C, right panel). Alternatively, $Q_{CO}$ might instead connect the intersections between the AF zone boundary and the underlying Fermi surface, the so-called hot spots where the effect of AF scattering and the pseudogap are maximal (30). However, the conventional expectation that the onset of CO above room temperature should gap the Fermi surface seems to contradict both scenarios, because the pseudogap opens only at the hot spots below 180 K, whereas no gapping is observed near $(\pi, 0)$ above the superconducting transition (1); this suggests that Fermi surface nesting might not be the origin of the CO. Unfortunately, however, this kind of comparison between temperature scales might be rendered inconclusive by the possibility that the CO never becomes sufficiently long-ranged, or large enough in amplitude, to induce a detectable reconstruction of the Fermi surface (at least in the absence of an applied magnetic field). Indeed, the widths of the CO peaks shown in Fig. 3, A and B, indicate a short correlation length (15 to 27 Å) (24), again similar to what has been observed in Bi-based cuprates (14–16). Perhaps further measurements, spanning larger doping ranges, will be able to test exactly which momentum states are involved in the CO, although the broadness of the CO peak in reciprocal space might ultimately limit the precision to which the location of $Q_{CO}$ on the Fermi surface can be determined.

The fact that CO never develops into a long-ranged electronic ground state might also hinder

the ability of transport or thermodynamic probes to detect it. However, we find that the presence of CO might be relevant to the interpretation of experiments that probe the inelastic excitations of $Nd_{2-x}Ce_xCuO_4$. We start by observing that the value of $Q_{CO}$ is consistent with the phonon anomaly near $H \approx 0.2$ observed by inelastic x-ray scattering in $Nd_{2-x}Ce_xCuO_4$ (31). More recently, Hinton et al. (32) reported time-resolved reflectivity studies that show the presence of a fluctuating order competing with superconductivity, although they could not determine which electronic degrees of freedom (i.e., charge or spin) were responsible for such order. Additionally, resonant inelastic x-ray scattering measurements (33, 34) have recently shown the presence of an inelastic mode—above a minimum energy transfer of $300 \pm 30$ meV [comparable to the pseudogap (30)]—which is distinct from the well-characterized AF fluctuations reminiscent of the Mott-insulating parent state (28, 33–35). Whereas Ishii et al. (34) ascribed this new mode to particle-hole charge excitations, Lee et al. (33) proposed that the mode might be the consequence of an unspecified broken symmetry—a scenario supported by their observation that this mode disappears above 270 K for $x = 0.166$. Our discovery of charge ordering in $Nd_{2-x}Ce_xCuO_4$ might provide the missing piece of information to interpret the aforementioned studies by identifying the actual broken symmetry.

Finally, on a fundamental level, some degree of electron-hole asymmetry should be expected in the cuprate phase diagram. In fact, whereas doped hole states below the charge transfer gap have a strong O-2p character, n-type doping creates low-energy electronic states of predominantly Cu-3d character in the upper Hubbard band (36–38). This dichotomy, together with recent RXS reports of a bond-centered CO in p-type ma-

terials (39), suggests that the n-type CO observed here may instead be centered on the Cu sites—an idea that requires further investigation. However, despite this underlying electron-hole asymmetry, the CO uncovered in $Nd_{2-x}Ce_xCuO_4$ by our study shows several similarities to its p-type equivalent, such as its direction, periodicity, and short correlation length (14, 15). In addition, our observation of a connection between the onset of CO and AF fluctuations suggests that the latter might generally lead to an accompanying intertwined charge order in unconventional superconductors, regardless of which orbitals are involved in the CO (40, 41). If such is the case, detailed studies will be necessary to understand the role of antiferromagnetism in charge order formation, perhaps even beyond the cuprates. Nonetheless, our discovery of charge ordering in n-type cuprates expands the universality of this phenomenon to the electron-doped side of the phase diagram, and provides a new avenue to understand its microscopic origin by exploiting the differences between p- and n-type cuprates.

## REFERENCES AND NOTES

1. N. P. Armitage, P. Fournier, R. L. Greene, *Rev. Mod. Phys.* **82**, 2421–2487 (2010).
2. J. M. Tranquada, B. J. Sternlieb, J. D. Axe, Y. Nakamura, S. Uchida, *Nature* **375**, 561–563 (1995).
3. P. Abbamonte et al., *Nat. Phys.* **1**, 155–158 (2005).
4. J. Fink et al., *Phys. Rev. B* **79**, 100502 (2009).
5. J. Fink et al., *Phys. Rev. B* **83**, 092503 (2011).
6. N. Doiron-Leyraud et al., *Nature* **447**, 565–568 (2007).
7. S. E. Sebastian et al., *Nat. Commun.* **2**, 471 (2011).
8. T. Wu et al., *Nature* **477**, 191–194 (2011).
9. G. Ghiringhelli et al., *Science* **337**, 821–825 (2012).
10. J. Chang et al., *Nat. Phys.* **8**, 871–876 (2012).
11. A. J. Achkar et al., *Phys. Rev. Lett.* **109**, 167001 (2012).
12. S. Blanco-Canosa et al., *Phys. Rev. Lett.* **110**, 187001 (2013).
13. S. Blanco-Canosa et al., *Phys. Rev. B* **90**, 054513 (2014).
14. R. Comin et al., *Science* **343**, 390–392 (2014).
15. E. H. da Silva Neto et al., *Science* **343**, 393–396 (2014).
16. M. Hashimoto et al., *Phys. Rev. B* **89**, 220511 (2014).
17. J. E. Hoffman et al., *Science* **295**, 466–469 (2002).
18. M. Vershinin et al., *Science* **303**, 1995–1998 (2004).
19. C. Howald, H. Eisaki, N. Kaneko, A. Kapitulnik, *Proc. Natl. Acad. Sci. U.S.A.* **100**, 9705–9709 (2003).
20. W. D. Wise et al., *Nat. Phys.* **4**, 696–699 (2008).
21. W. Tabis et al., http://arxiv.org/abs/1404.7658 (2014).
22. C. V. Parker et al., *Nature* **468**, 677–680 (2010).
23. M. Hücker et al., *Phys. Rev. B* **90**, 054514 (2014).
24. See supplementary materials on *Science* Online.
25. T. Helm et al., *Phys. Rev. Lett.* **103**, 157002 (2009).
26. T. Helm et al., *Phys. Rev. Lett.* **105**, 247002 (2010).
27. Y. Onose, Y. Taguchi, K. Ishizaka, Y. Tokura, *Phys. Rev. B* **69**, 024504 (2004).
28. E. M. Motoyama et al., *Nature* **445**, 186–189 (2007).
29. B. Kyung, V. Hankevych, A.-M. Daré, A.-M. S. Tremblay, *Phys. Rev. Lett.* **93**, 147004 (2004).
30. N. P. Armitage et al., *Phys. Rev. Lett.* **87**, 147003 (2001).
31. M. d'Astuto et al., *Phys. Rev. Lett.* **88**, 167002 (2002).
32. J. P. Hinton et al., *Phys. Rev. Lett.* **110**, 217002 (2013).
33. W. S. Lee et al., *Nat. Phys.* **10**, 883–889 (2014).
34. K. Ishii et al., *Nat. Commun.* **5**, 3714 (2014).
35. K. Yamada et al., *Phys. Rev. Lett.* **90**, 137004 (2003).
36. J. Zaanen, G. A. Sawatzky, J. W. Allen, *Phys. Rev. Lett.* **55**, 418–421 (1985).
37. C. T. Chen et al., *Phys. Rev. Lett.* **66**, 104–107 (1991).
38. E. Pellegrin et al., *Phys. Rev. B* **47**, 3354–3367 (1993).
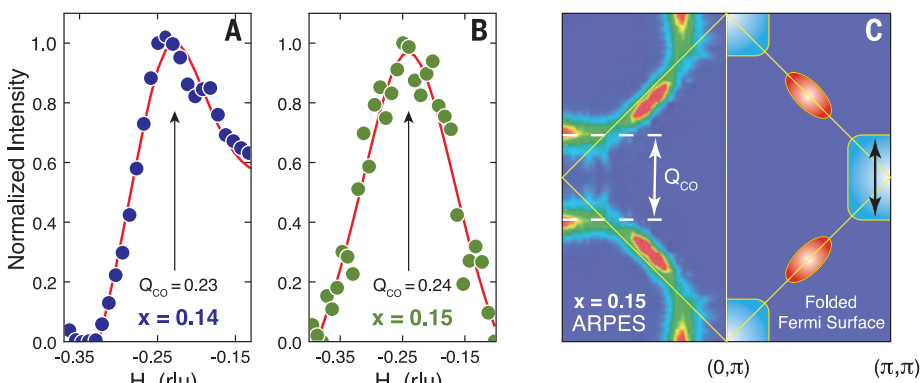
**Fig. 3. Electronic origin of the CO.** (**A** and **B**) CO peak extracted by subtraction of the highest-temperature θ scan from an average of the lowest-temperature θ scans (22 to 180 K) (24). A fit of the data to a Lorentzian plus linear background function (red line) is used to indicate the *H* value of highest intensity, which is $-0.23 \pm 0.04$ rlu for the $x = 0.14$ sample (A) and $-0.24 \pm 0.04$ rlu for the $x = 0.15$ sample (B). The extracted peaks in (A) and (B) are normalized to their respective maxima. (**C**) Fermi surface of $Nd_{2-x}Ce_xCuO_4$ ($x = 0.15$) measured by ARPES (30) (left) and a schematic of the expected Fermi surface reconstruction (right) due to AF folding (yellow diamond). The folded Fermi surface is composed of hole (red) and electron (cyan) pockets. The arrows (white and black) and dashed lines represent $Q_{CO} = 0.24$ rlu, and connect either the parallel segments of the Fermi surface near $(\pi, 0)$ or the intersection with the AF zone boundary.

39. R. Comin *et al.*, http://arxiv.org/abs/1402.5415 (2014).
40. E. Fradkin, S. A. Kivelson, *Nat. Phys.* **8**, 864–866 (2012).
41. J. C. S. Davis, D.-H. Lee, *Proc. Natl. Acad. Sci. U.S.A.* **110**, 17623–17630 (2013).

## APPLIED PHYSICS

# Semiconductor double quantum dot micromaser

Y.-Y. Liu,[1] J. Stehlik,[1] C. Eichler,[1] M. J. Gullans,[2] J. M. Taylor,[2,3] J. R. Petta[1,4]*

The coherent generation of light, from masers to lasers, relies upon the specific structure of the individual emitters that lead to gain. Devices operating as lasers in the few-emitter limit provide opportunities for understanding quantum coherent phenomena, from terahertz sources to quantum communication. Here we demonstrate a maser that is driven by single-electron tunneling events. Semiconductor double quantum dots (DQDs) serve as a gain medium and are placed inside a high-quality factor microwave cavity. We verify maser action by comparing the statistics of the emitted microwave field above and below the maser threshold.

A conventional laser uses an ensemble of atoms that are pumped into the excited state to achieve population inversion (*1*, *2*). Enabled by advances in semiconductor device technology, semiconductor lasers quickly evolved from p-i-n junctions (*3*, *4*), to quantum well structures (*5*) and quantum cascade lasers (QCLs) (*6*). In QCLs, an electrical bias is applied across exquisitely engineered multiple quantum well structures, resulting in cascaded intraband transitions between confined two-dimensional electronic states that lead to photon emission (*7*). However, QCL emission frequencies are set by heterostructure growth profiles and cannot be easily tuned in situ. At the same time, in atomic physics, researchers demonstrated a single-atom maser, where atoms prepared in the excited state transit through a microwave cavity for a precisely controlled period of time, such that the atom "swaps" its excitation to the microwave cavity, generating a large photon field (*8*). These early experiments were extended to a single atom trapped in a high-finesse optical cavity (*9*), as well as condensed-matter systems, where artificial atoms were strongly coupled to cavities (*10–14*).

Here we demonstrate a maser that is driven by single-electron tunneling events. The gain medium consists of semiconductor double quantum dots (DQDs) that support zero-dimensional electronic states (*15*). Electronic tunneling through the DQDs generates photons that are coupled to a cavity mode (*16*). In contrast to optically pumped systems, population inversion is generated in the DQD system through the application of a bias voltage that results in sequential single-electron tunneling.

The maser consists of two semiconductor DQDs (referred to as the left DQD and right DQD, Fig. 1), which are electric-dipole coupled to a microwave cavity. The cavity is formed from a half-wavelength ($\lambda/2$) superconducting Nb transmission line resonator with a center frequency $f_c$ = 7880.55 MHz and a loaded quality factor $Q_c \approx 3000$ (*17*, *18*). Two lithographically defined InAs nanowire DQDs serve as the maser gain medium (*16*, *19*). Each DQD is fabricated by placing a single InAs nanowire over five Ti/Au bottom gate electrodes (Fig. 1C) (*20*, *21*). The bottom gates create a tunable DQD confinement potential in the nanowire (*21*). Electrostatically defined DQDs, often regarded as artificial molecules (*15*), are a unique gain medium. They are fully reconfigurable, with electronic transitions that can be tuned from gigahertz to terahertz frequencies.

A source-drain bias voltage $V_{SD}$ = 2 mV is applied across the DQDs to drive a current. The energy levels of each DQD can be separately tuned and are described by the left (right) DQD detuning $\varepsilon_L$ ($\varepsilon_R$). Current will flow in a nanowire DQD through a series of downhill (in energy) single-electron tunneling events (see level diagrams in Fig. 1B). In contrast with quantum well structures, current results from single-electron tunneling events between electrically tunable zero-dimensional states in the DQD (*15*, *22*). Electron tunneling results in microwave gain, which is accessed by measuring the transmission through the cavity (*16*).

To measure the gain, the cavity is driven with a coherent field at frequency $f_{in} = f_c$ with a power $P_{in}$. Measurements of the output power $P_{out}$ yield the power gain $G = CP_{out}/P_{in}$, where $C$ is a normalization constant set such that $G = 1$ when both DQDs are in Coulomb blockade (no current flow) (*16*, *23*). With $V_{SD}$ = 0, charge dynamics within the DQD result in an effective microwave admittance that damps the electromagnetic field inside the cavity, yielding $G < 1$ (*18*, *24*, *25*). Application of a source-drain bias that drives sequential tunneling through the DQD can lead to gain in the cavity transmission, $G > 1$ (*16*). In Fig. 1D, we plot $G$ as a function of $\varepsilon_L$ for $V_{SD}$ = 2 mV and $f_{in} = f_c$. For downhill electron tunneling ($\varepsilon_L > 0$), we measure a maximum gain $G \approx 7$ (*23*). In contrast, for $\varepsilon_L < 0$, the left DQD can absorb a photon from the cavity, leading to loss $G \approx 0.2$ (*18*, *25*). These data are acquired with the right DQD configured in Coulomb blockade such that the current is zero (*15*). For simplicity, we refer to a DQD as "on" when its detuning is set to achieve maximum gain and "off" when the DQD is configured in Coulomb blockade with $G = 1$.

We investigate the cavity response by measuring $G$ as a function of $f_{in}$ with $P_{in}$ = –120 dBm (Fig. 2). The black curve is the "cold cavity transmission" obtained with both DQDs configured in the off state, where the maximum $G = 1$. Here the gain curve is a Lorentzian with a width set by the cavity decay rate $\kappa/2\pi$ = 2.6 MHz. When $\varepsilon_L$ is set to the gain peak shown in Fig. 1D, we observe a maximum $G \approx 16$ at $f_{in}$ = 7880.30 MHz. Similarly, with the right DQD on and the left DQD off, we observe a maximum $G \approx 6$ at $f_{in}$ = 7880.41 MHz. In both configurations, the observed gain rate is too small to reach the maser threshold. In contrast, the red curve in Fig. 2 shows the gain curve with both DQDs in the on state. Here the cavity response is sharply peaked at $f_{in}$ = 7880.25 MHz, yielding a maximum gain $G \approx 1000$, which is much larger than the product of the individual gains.

We next examine the characteristics of the device in free-running mode (with no cavity drive tone). Figure 3 shows the power spectral density $S(f)$ of microwave radiation emitted from the cavity in the on/on configuration. The spectrum is

[1]Department of Physics, Princeton University, Princeton, NJ 08544, USA. [2]Joint Quantum Institute, University of Maryland–National Institute of Standards and Technology, College Park, MD 20742, USA. [3]Joint Center for Quantum Information and Computer Science, University of Maryland and NIST, College Park, MD 20742, USA. [4]Department of Physics, University of California, Santa Barbara, CA 93106, USA.
*Corresponding author. E-mail: petta@princeton.edu

# Supplementary Materials for

## Charge ordering in the electron-doped superconductor $Nd_{2-x}Ce_xCuO_4$

Eduardo H. da Silva Neto,* Riccardo Comin, Feizhou He, Ronny Sutarto, Yeping Jiang, Richard L. Greene, George A. Sawatzky, Andrea Damascelli*

*Corresponding author. E-mail: ehda@physics.ubc.ca (E.H.d.S.N.); damascelli@physics.ubc.ca (A.D.)

**This PDF file includes:**

**Materials and Methods**

RXS measurements were performed at the REIXS beamline of the Canadian Light Source, using a 4-circle diffractometer (*42*). Reciprocal-space scans were acquired by rocking the sample angle ($\theta$) at fixed detector position ($\theta_{det}$=170°), in the temperature range 22 to 420 K. The incoming photon polarization was set vertical to the scattering plane ($\sigma$ polarization). The samples were pre-oriented using Laue diffraction and mounted with either **a** or **b** axis in the scattering plane. Four samples were measured in the doping range $x = 0.14 \pm 0.01$ to $x = 0.15 \pm 0.01$. No qualitative differences were observed between measurements done on samples cleaved in situ and samples where no surface preparation was done. In all cases resonant CO peaks were detected with wavevectors and temperature dependences similar to those reported in the text. The crystals were grown by the flux method and annealed for two days at the appropriate temperature to render them superconducting (*1*). The Ce concentration of the crystals was determined using wavelength dispersive x-ray (WDX) analysis. The $T_c$ onset determined from resistivity measurements is near 21 K for both samples, and zero-field-cooled susceptibility measurements indicate full superconductivity. Hall-effect measurements on the $x = 0.14$ sample are compatible with the doping indicated by WDX within the error limits ±0.01.

**Supplementary Text**

Energy Dependence of the CO Scattering Peak

Measurements performed with the photon energy set to the Ce-M edges (884.3 eV and 901.9 eV), Nd-*M* edges (978.2 eV and 998.8 eV), and O-*K* edge (530.5 eV) did not show any diffraction peaks in the $\theta$-scans. However, given the rich structure of the O-*K* absorption edge in the cuprates, our limited measurements at this energy are far from sufficient to rule out the presence of a CO peak at that absorption peak. On the other hand, diffraction peaks (at a wavevector of H ≈ ± 0.24) were readily detected when the photon energy was tuned near the Cu-$L_3$ edge at 931.5 eV (Fig. S1). Due to a more sloped background for the positive-H $\theta$-scans (Fig. S1), for most of this study we focused our measurements on the H < 0 section of reciprocal space. The resonance energy profile of the scattering peak (obtained after background subtraction) is shown in Fig. S2.

Temperature Dependence of the Charge Ordering

Figure 2C in the manuscript shows the extracted temperature dependence of the CO peak. The full set of $\theta$-scans from which Fig. 2C was generated is displayed in Fig. S3. It can already be seen in the raw data that CO onsets in the temperature range between 300 K and 340 K. More importantly, for both dopings ($x = 0.14$ and $x = 0.15$) a robust CO peak is already observed at 180 K, which is above the pseudogap temperature, 80-170K in the $x = 0.14$-0.15 doping range (*1,27,28*). This confirms that the CO onsets at much higher temperatures than the pseudogap – a key finding of our work.

The shape of the background (420 K) is a combination of systematic effects, but it is mostly determined by the angular dependence of the fluorescence emission, making it difficult to interpret quantitatively. On a qualitative account, the $\theta$-scans we performed span an angular range of 50°, so small variations in the background are expected. Particularly on the far side the incoming and take-off beams approach grazing angles, causing a stronger sensitivity of the background signal to the relative position of the beam on the sample and to inhomogeneities due to the larger (surface-projected) effective beam spot. Given that no two measured samples have identical geometrical shapes, the fluorescence background observed in the $\theta$-scans is expected to vary between measurements. Indeed such a variation can be seen between the $\theta$-scans for $x = 0.14$ and $x = 0.15$ samples (Fig. 1C-D, Fig. 2A-B and Fig. S3), which show backgrounds with different slopes. To a much smaller degree a similar effect is also observed as a function of temperature due to thermal drift. To minimize this systematic effect the sample position was adjusted at each temperature in order to maintain it constant. Nevertheless, small variations of the sample position (in the order of 50 μm) are inevitable and therefore the $\theta$-scans in Fig. S3 show slight differences in the background as a function of temperature. Indeed this kind of effect has been observed in YBCO, BSCCO 2201, and BSCCO 2212 measurements performed in this scattering chamber, although perhaps less apparent in the case of YBCO due to the higher signal-to-background ratio of the CO peak.

To extract the value of $Q_{CO}$ reported in the text and in Fig. 3A-B, we subtract the highest temperature $\theta$-scan (420 K) from an average of the lowest temperature data (22 K to 180 K). The averaging of the lowest temperature scans is used to minimize the differences in the background induced by thermal drift which could skew the $Q_{CO}$ value extracted from the data. Despite this averaging an asymmetry is observed in the peak of Fig. 3A, which originates from the background systematics mentioned above.

To extract the temperature dependence of the CO peak we need to determine a temperature independent background. However, choosing a single temperature as the background would have biased the determination of an onset temperature. Therefore the background used for subtraction in Fig. 2C is obtained from a polynomial fit to the tails ($H < -0.32$ and $H > -0.13$, e.g. excluding the peak region) of the temperature-averaged $\theta$-scans. Remarkably this polynomial line shape (red line in Fig. S4A-B) closely matches the high-temperature $\theta$-scans (see for example 380 K for $x = 0.14$ sample, Fig. S4A). This unique line shape is then subtracted from the total signal for each temperature in order to isolate the CO peak. The CO amplitude (and accompanying error bars) in Fig. 2C are obtained from a Lorentzian fit to the background-subtracted $\theta$-scans (Fig. S4C). Clearly a Lorentzian does not accurately fit the extracted peak, and we only use the fit to obtain a measure of the peak height, while discarding other fitting parameters such as the width. Of course a fit to a Lorentzian function plus a linear background seems to better capture the background-subtracted peak (Fig. S4C), and it yields a similar temperature dependence as in Fig. 2C (see Fig. S4D for comparison). Given that the two methods are equivalent, we chose to use the single Lorentzian fit, since it is the minimal model to fit a peak, and yields (larger) error bars that better reflect the experimental uncertainty. We conclude that the temperature evolution in Fig. 2C is robust to the choice of fitting method, and that it simply summarizes the behavior already seen in the raw data (Fig. S4).

## Correlation Length of the Charge Ordering

To estimate the real-space correlation length, $\xi$, of the charge order we need to determine the width of the CO peak in reciprocal space. Because of the small amplitude of the scattering signal in relation to the fluorescence background, we find no statistical difference between fitting the extracted peaks with a Lorentzian or a Gaussian function. Using either fitting function we find that the half width at half maximum (HWHM) values range from 0.04 to 0.07 rlu as obtained from fitting the background-subtracted peak for all dopings and temperatures reported here. We note that this HWHM is similar to the values reported for $Bi_2Sr_{2-x}La_xCuO_{6+\delta}$ (~0.04 to 0.05 rlu). Assuming that the peak has a Gaussian lineshape, we obtain the values for $\xi$ reported in the text (15 to 27 Å). If a Lorentzian function is assumed instead, then the $\xi$ values above should be divided by $2(\ln2)^{1/2} = 1.66$ – reflecting the difference in the functional form for the density-density correlation function: a simple exponential (Lorentzian in Fourier space) in one case, and a Gaussian (also a Gaussian in Fourier space) in the other.
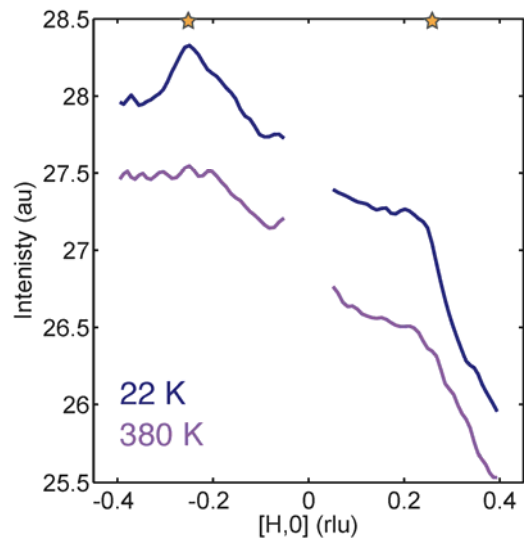
**Fig. S1**

On-resonance (Cu-$L_3$ edge, 931.5 eV) $\theta$-scans for an $x = 0.14$ sample at 22 K (blue) and 380 K (purple) showing the presence of a scattering peaks for $H \approx \pm 0.24$ (yellow stars) at low temperature. The intensity is proportional to the multi-channel plate (MCP) detector reading normalized by the beam flux.
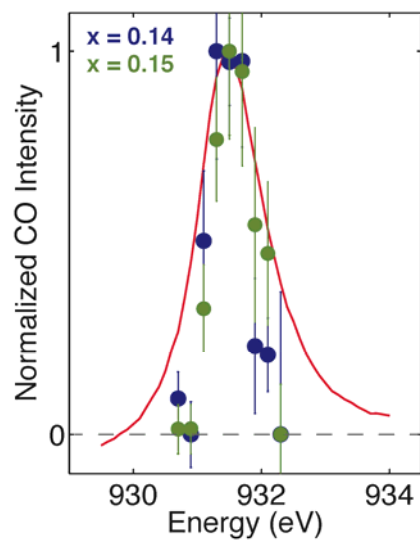
**Fig. S2**

Resonance profile at $Q_{CO}$ obtained after background subtraction for $x = 0.14$ (blue) and $x = 0.15$ (green) samples, superimposed on the Cu-$L_3$ absorption edge (red line).
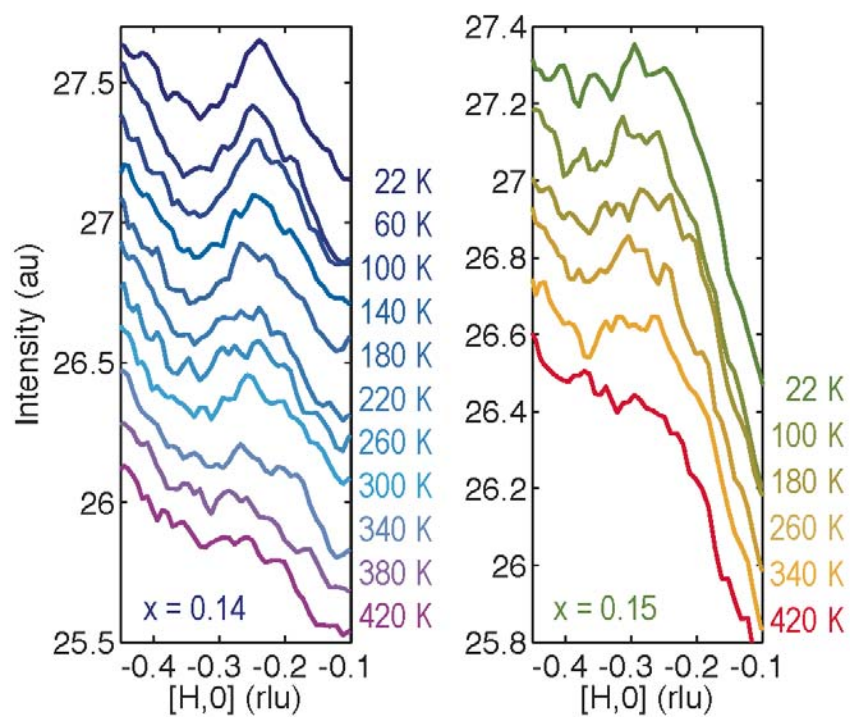
**Fig. S3**

Temperature dependence of $\theta$-scans for $x = 0.14$ and $x = 0.15$ samples. The curves were vertically offset for clarity. Note that for both samples the CO scattering peak first develops around 340 K, and it is clearly visible at 180 K.
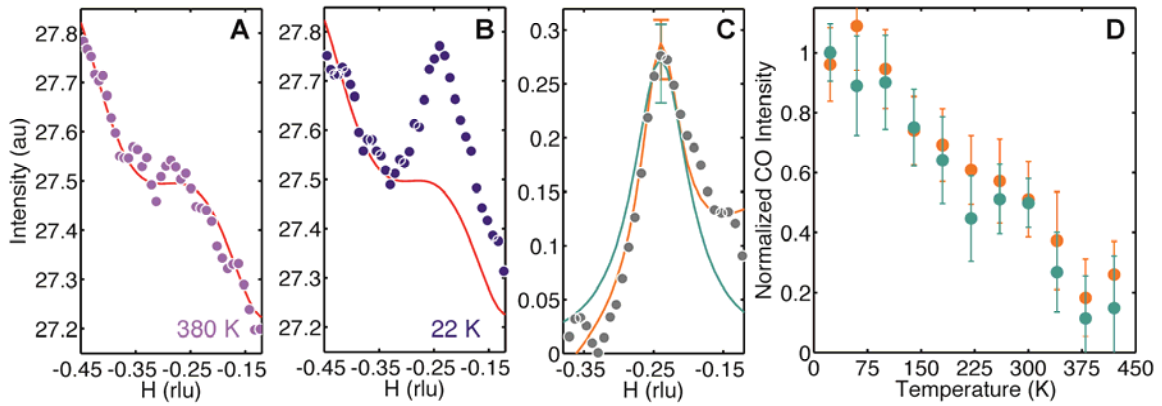
**Fig. S4**

(**A-B**) $\theta$-scans for $x = 0.14$ sample at 380 K (purple) and 22 K (blue), respectively. The background function obtained from a polynomial fit to the temperature-averaged $\theta$-scans is also shown (red, see text for details). (**C**) Extracted CO peak (gray) and fit to a Lorentzian function with (orange) and without (blue) linear background. (**D**) Comparison between the temperature dependence extracted using the two different fitting procedures.

**References**

1. N. P. Armitage, P. Fournier, R. L. Greene, Progress and perspectives on electron-doped cuprates. *Rev. Mod. Phys.* **82**, 2421–2487 (2010). doi:10.1103/RevModPhys.82.2421

2. J. M. Tranquada, B. J. Sternlieb, J. D. Axe, Y. Nakamura, S. Uchida, Evidence for stripe correlations of spins and holes in copper oxide superconductors. *Nature* **375**, 561–563 (1995). doi:10.1038/375561a0

3. P. Abbamonte, A. Rusydi, S. Smadici, G. D. Gu, G. A. Sawatzky, D. L. Feng, Spatially modulated 'Mottness' in $La_{2-x}Ba_xCuO_4$. *Nat. Phys.* **1**, 155–158 (2005). doi:10.1038/nphys178

4. J. Fink, E. Schierle, E. Weschke, J. Geck, D. Hawthorn, V. Soltwisch, H. Wadati, H.-H. Wu, H. Dürr, N. Wizent, B. Büchner, G. Sawatzky, Charge ordering in $La_{1.8-x}Eu_{0.2}Sr_xCuO_4$ studied by resonant soft x-ray diffraction. *Phys. Rev. B* **79**, 100502 (2009). doi:10.1103/PhysRevB.79.100502

5. J. Fink, V. Soltwisch, J. Geck, E. Schierle, E. Weschke, B. Büchner, Phase diagram of charge order in $La_{1.8-x}Eu_{0.2}Sr_xCuO_4$ from resonant soft x-ray diffraction. *Phys. Rev. B* **83**, 092503 (2011). doi:10.1103/PhysRevB.83.092503

6. N. Doiron-Leyraud, C. Proust, D. LeBoeuf, J. Levallois, J. B. Bonnemaison, R. Liang, D. A. Bonn, W. N. Hardy, L. Taillefer, Quantum oscillations and the Fermi surface in an underdoped high-$T_c$ superconductor. *Nature* **447**, 565–568 (2007). Medline doi:10.1038/nature05872

7. S. E. Sebastian, N. Harrison, M. M. Altarawneh, R. Liang, D. A. Bonn, W. N. Hardy, G. G. Lonzarich, Chemical potential oscillations from nodal Fermi surface pocket in the underdoped high-temperature superconductor $Yba_2Cu_3O_{6+x}$. *Nat. Commun.* **2**, 471 (2011). Medline doi:10.1038/ncomms1468

8. T. Wu, H. Mayaffre, S. Krämer, M. Horvatić, C. Berthier, W. N. Hardy, R. Liang, D. A. Bonn, M. H. Julien, Magnetic-field-induced charge-stripe order in the high-temperature superconductor $YBa_2Cu_3O_y$. *Nature* **477**, 191–194 (2011). Medline doi:10.1038/nature10345

9. G. Ghiringhelli, M. Le Tacon, M. Minola, S. Blanco-Canosa, C. Mazzoli, N. B. Brookes, G. M. De Luca, A. Frano, D. G. Hawthorn, F. He, T. Loew, M. Moretti Sala, D. C. Peets, M. Salluzzo, E. Schierle, R. Sutarto, G. A. Sawatzky, E. Weschke, B. Keimer, L. Braicovich, Long-range incommensurate charge fluctuations in (Y,Nd)Ba$_2$Cu$_3$O$_{6+x}$. *Science* **337**, 821–825 (2012). Medline doi:10.1126/science.1223532

10. J. Chang, E. Blackburn, A. T. Holmes, N. B. Christensen, J. Larsen, J. Mesot, R. Liang, D. A. Bonn, W. N. Hardy, A. Watenphul, M. Zimmermann, E. M. Forgan, S. M. Hayden, Direct observation of competition between superconductivity and charge density wave order in YBa$_2$Cu$_3$O$_{6.67}$. *Nat. Phys.* **8**, 871–876 (2012). doi:10.1038/nphys2456

11. A. J. Achkar, R. Sutarto, X. Mao, F. He, A. Frano, S. Blanco-Canosa, M. Le Tacon, G. Ghiringhelli, L. Braicovich, M. Minola, M. Moretti Sala, C. Mazzoli, R. Liang, D. A. Bonn, W. N. Hardy, B. Keimer, G. A. Sawatzky, D. G. Hawthorn, Distinct charge orders in the planes and chains of ortho-III-ordered YBa$_2$Cu$_3$O$_{6+\delta}$ superconductors identified by resonant elastic x-ray scattering. *Phys. Rev. Lett.* **109**, 167001 (2012). Medline doi:10.1103/PhysRevLett.109.167001

12. S. Blanco-Canosa, A. Frano, T. Loew, Y. Lu, J. Porras, G. Ghiringhelli, M. Minola, C. Mazzoli, L. Braicovich, E. Schierle, E. Weschke, M. Le Tacon, B. Keimer, Momentum-dependent charge correlations in YBa$_2$Cu$_3$O$_{6+\delta}$ superconductors probed by resonant X-ray scattering: Evidence for three competing phases. *Phys. Rev. Lett.* **110**, 187001 (2013). Medline doi:10.1103/PhysRevLett.110.187001

13. S. Blanco-Canosa, A. Frano, E. Schierle, J. Porras, T. Loew, M. Minola, M. Bluschke, E. Weschke, B. Keimer, M. Le Tacon, Resonant x-ray scattering study of charge-density wave correlations in YBa$_2$Cu$_3$O$_{6+x}$. *Phys. Rev. B* **90**, 054513 (2014). doi:10.1103/PhysRevB.90.054513

14. R. Comin, A. Frano, M. M. Yee, Y. Yoshida, H. Eisaki, E. Schierle, E. Weschke, R. Sutarto, F. He, A. Soumyanarayanan, Y. He, M. Le Tacon, I. S. Elfimov, J. E. Hoffman, G. A. Sawatzky, B. Keimer, A. Damascelli, Charge order driven by Fermi-arc instability in Bi$_2$Sr$_{2-x}$La$_x$CuO$_{6+\delta}$. *Science* **343**, 390–392 (2014). Medline doi:10.1126/science.1242996

15. E. H. da Silva Neto, P. Aynajian, A. Frano, R. Comin, E. Schierle, E. Weschke, A. Gyenis, J. Wen, J. Schneeloch, Z. Xu, S. Ono, G. Gu, M. Le Tacon, A. Yazdani, Ubiquitous interplay between charge ordering and high-temperature superconductivity in cuprates. *Science* **343**, 393–396 (2014). Medline doi:10.1126/science.1243479

16. M. Hashimoto, G. Ghiringhelli, W.-S. Lee, G. Dellea, A. Amorese, C. Mazzoli, K. Kummer, N. B. Brookes, B. Moritz, Y. Yoshida, H. Eisaki, Z. Hussain, T. P. Devereaux, Z.-X. Shen, L. Braicovich, Direct observation of bulk charge modulations in optimally doped $Bi_{1.5}Pb_{0.6}Sr_{1.54}CaCu_2O_{8+\delta}$. *Phys. Rev. B* **89**, 220511 (2014). doi:10.1103/PhysRevB.89.220511

17. J. E. Hoffman, E. W. Hudson, K. M. Lang, V. Madhavan, H. Eisaki, S. Uchida, J. C. Davis, A four unit cell periodic pattern of quasi-particle states surrounding vortex cores in $Bi_2Sr_2CaCu_2O_{8+\delta}$. *Science* **295**, 466–469 (2002). Medline doi:10.1126/science.1066974

18. M. Vershinin, S. Misra, S. Ono, Y. Abe, Y. Ando, A. Yazdani, Local ordering in the pseudogap state of the high-$T_c$ superconductor $Bi_2Sr_2CaCu_2O_{8+\delta}$. *Science* **303**, 1995–1998 (2004). Medline doi:10.1126/science.1093384

19. C. Howald, H. Eisaki, N. Kaneko, A. Kapitulnik, Coexistence of periodic modulation of quasiparticle states and superconductivity in $Bi_2Sr_2CaCu_2O_{8+\delta}$. *Proc. Natl. Acad. Sci. U.S.A.* **100**, 9705–9709 (2003). Medline doi:10.1073/pnas.1233768100

20. W. D. Wise, M. C. Boyer, K. Chatterjee, T. Kondo, T. Takeuchi, H. Ikuta, Y. Wang, E. W. Hudson, Charge-density-wave origin of cuprate checkerboard visualized by scanning tunnelling microscopy. *Nat. Phys.* **4**, 696–699 (2008). doi:10.1038/nphys1021

21. W. Tabis *et al*., Charge order and its connection with Fermi-liquid charge transport in a pristine high-$T_c$ cuprate. *Nat. Commun.* **5**, 5875 (2014). doi:10.1038/ncomms6875

22. C. V. Parker, P. Aynajian, E. H. da Silva Neto, A. Pushp, S. Ono, J. Wen, Z. Xu, G. Gu, A. Yazdani, Fluctuating stripes at the onset of the pseudogap in the high-$T_c$ superconductor $Bi_2Sr_2CaCu_2O_{8+x}$. *Nature* **468**, 677–680 (2010). Medline doi:10.1038/nature09597

23. M. Hücker, N. B. Christensen, A. T. Holmes, E. Blackburn, E. M. Forgan, R. Liang, D. A. Bonn, W. N. Hardy, O. Gutowski, M. Zimmermann, S. M. Hayden, J. Chang, Competing

charge, spin, and superconducting orders in underdoped $YBa_2Cu_3O_y$. *Phys. Rev. B* **90**, 054514 (2014). [doi:10.1103/PhysRevB.90.054514](doi:10.1103/PhysRevB.90.054514)

24. See supplementary materials on *Science* Online.

25. T. Helm, M. V. Kartsovnik, M. Bartkowiak, N. Bittner, M. Lambacher, A. Erb, J. Wosnitza, R. Gross, Evolution of the Fermi surface of the electron-doped high-temperature superconductor $Nd_{2-x}Ce_xCuO_4$ revealed by Shubnikov-de Haas oscillations. *Phys. Rev. Lett.* **103**, 157002 (2009). [Medline](Medline) [doi:10.1103/PhysRevLett.103.157002](doi:10.1103/PhysRevLett.103.157002)

26. T. Helm, M. V. Kartsovnik, I. Sheikin, M. Bartkowiak, F. Wolff-Fabris, N. Bittner, W. Biberacher, M. Lambacher, A. Erb, J. Wosnitza, R. Gross, Magnetic breakdown in the electron-doped cuprate superconductor $Nd_{2-x}Ce_xCuO_4$: The reconstructed Fermi surface survives in the strongly overdoped regime. *Phys. Rev. Lett.* **105**, 247002 (2010). [Medline](Medline) [doi:10.1103/PhysRevLett.105.247002](doi:10.1103/PhysRevLett.105.247002)

27. Y. Onose, Y. Taguchi, K. Ishizaka, Y. Tokura, Charge dynamics in underdoped $Nd_{2-x}Ce_xCuO_4$: Pseudogap and related phenomena. *Phys. Rev. B* **69**, 024504 (2004). [doi:10.1103/PhysRevB.69.024504](doi:10.1103/PhysRevB.69.024504)

28. E. M. Motoyama, G. Yu, I. M. Vishik, O. P. Vajk, P. K. Mang, M. Greven, Spin correlations in the electron-doped high-transition-temperature superconductor $Nd_{2-x}Ce_xCuO_{4+\delta}$. *Nature* **445**, 186–189 (2007). [Medline](Medline) [doi:10.1038/nature05437](doi:10.1038/nature05437)

29. B. Kyung, V. Hankevych, A.-M. Daré, A.-M. S. Tremblay, Pseudogap and spin fluctuations in the normal state of the electron-doped cuprates. *Phys. Rev. Lett.* **93**, 147004 (2004). [Medline](Medline) [doi:10.1103/PhysRevLett.93.147004](doi:10.1103/PhysRevLett.93.147004)

30. N. P. Armitage, D. H. Lu, C. Kim, A. Damascelli, K. M. Shen, F. Ronning, D. L. Feng, P. Bogdanov, Z. X. Shen, Y. Onose, Y. Taguchi, Y. Tokura, P. K. Mang, N. Kaneko, M. Greven, Anomalous electronic structure and pseudogap effects in $Nd_{1.85}Ce_{0.15}CuO_4$. *Phys. Rev. Lett.* **87**, 147003 (2001). [Medline](Medline) [doi:10.1103/PhysRevLett.87.147003](doi:10.1103/PhysRevLett.87.147003)

31. M. d'Astuto, P. K. Mang, P. Giura, A. Shukla, P. Ghigna, A. Mirone, M. Braden, M. Greven, M. Krisch, F. Sette, Anomalous dispersion of longitudinal optical phonons in $Nd_{1.86}Ce_{0.14}CuO_{4+\delta}$ determined by inelastic x-ray scattering. *Phys. Rev. Lett.* **88**, 167002 (2002). [Medline](Medline) [doi:10.1103/PhysRevLett.88.167002](doi:10.1103/PhysRevLett.88.167002)

32. J. P. Hinton, J. D. Koralek, G. Yu, E. M. Motoyama, Y. M. Lu, A. Vishwanath, M. Greven, J. Orenstein, Time-resolved optical reflectivity of the electron-doped $Nd_{2-x}Ce_xCuO_{4+\delta}$ cuprate superconductor: Evidence for an interplay between competing orders. *Phys. Rev. Lett.* **110**, 217002 (2013). [Medline](Medline) [doi:10.1103/PhysRevLett.110.217002](doi:10.1103/PhysRevLett.110.217002)

33. W. S. Lee, J. J. Lee, E. A. Nowadnick, S. Gerber, W. Tabis, S. W. Huang, V. N. Strocov, E. M. Motoyama, G. Yu, B. Moritz, H. Y. Huang, R. P. Wang, Y. B. Huang, W. B. Wu, C. T. Chen, D. J. Huang, M. Greven, T. Schmitt, Z. X. Shen, T. P. Devereaux, Asymmetry of collective excitations in electron- and hole-doped cuprate superconductors. *Nat. Phys.* **10**, 883–889 (2014). [doi:10.1038/nphys3117](doi:10.1038/nphys3117)

34. K. Ishii, M. Fujita, T. Sasaki, M. Minola, G. Dellea, C. Mazzoli, K. Kummer, G. Ghiringhelli, L. Braicovich, T. Tohyama, K. Tsutsumi, K. Sato, R. Kajimoto, K. Ikeuchi, K. Yamada, M. Yoshida, M. Kurooka, J. Mizuki, High-energy spin and charge excitations in electron-doped copper oxide superconductors. *Nat. Commun.* **5**, 3714 (2014). [Medline](Medline) [doi:10.1038/ncomms4714](doi:10.1038/ncomms4714)

35. K. Yamada, K. Kurahashi, T. Uefuji, M. Fujita, S. Park, S. H. Lee, Y. Endoh, Commensurate spin dynamics in the superconducting state of an electron-doped cuprate superconductor. *Phys. Rev. Lett.* **90**, 137004 (2003). [Medline](Medline) [doi:10.1103/PhysRevLett.90.137004](doi:10.1103/PhysRevLett.90.137004)

36. J. Zaanen, G. A. Sawatzky, J. W. Allen, Band gaps and electronic structure of transition-metal compounds. *Phys. Rev. Lett.* **55**, 418–421 (1985). [Medline](Medline) [doi:10.1103/PhysRevLett.55.418](doi:10.1103/PhysRevLett.55.418)

37. C. T. Chen, F. Sette, Y. Ma, M. S. Hybertsen, E. B. Stechel, W. M. Foulkes, M. Schulter, S. W. Cheong, A. S. Cooper, L. W. Rupp Jr., B. Batlogg, Y. L. Soo, Z. H. Ming, A. Krol, Y. H. Kao, Electronic states in $La_{2-x}Sr_xCuO_{4+\delta}$ probed by soft-x-ray absorption. *Phys. Rev. Lett.* **66**, 104–107 (1991). [Medline](Medline) [doi:10.1103/PhysRevLett.66.104](doi:10.1103/PhysRevLett.66.104)

38. E. Pellegrin, N. Nücker, J. Fink, S. Molodtsov, A. Gutiérrez, E. Navas, O. Strebel, Z. Hu, M. Domke, G. Kaindl, S. Uchida, Y. Nakamura, J. Markl, M. Klauda, G. Saemann-Ischenko, A. Krol, J. Peng, Z. Li, R. Greene, Orbital character of states at the Fermi level in $La_{2-x}Sr_xCuO_4$ and $R_{2-x}Ce_xCuO_4$ (R=Nd,Sm). *Phys. Rev. B* **47**, 3354–3367 (1993). [doi:10.1103/PhysRevB.47.3354](doi:10.1103/PhysRevB.47.3354)

39. R. Comin *et al*., http://arxiv.org/abs/1402.5415 (2014).

40. E. Fradkin, S. A. Kivelson, High-temperature superconductivity: Ineluctable complexity. *Nat. Phys.* **8**, 864–866 (2012). [doi:10.1038/nphys2498](doi:10.1038/nphys2498)

41. J. C. S. Davis, D.-H. Lee, Concepts relating magnetic interactions, intertwined electronic orders, and strongly correlated superconductivity. *Proc. Natl. Acad. Sci. U.S.A.* **110**, 17623–17630 (2013). [Medline](Medline) [doi:10.1073/pnas.1316512110](doi:10.1073/pnas.1316512110)

42. D. G. Hawthorn, F. He, L. Venema, H. Davis, A. J. Achkar, J. Zhang, R. Sutarto, H. Wadati, A. Radi, T. Wilson, G. Wright, K. M. Shen, J. Geck, H. Zhang, V. Novák, G. A. Sawatzky, An in-vacuum diffractometer for resonant elastic soft x-ray scattering. *Rev. Sci. Instrum.* **82**, 073104 (2011). [Medline](Medline) [doi:10.1063/1.3607438](doi:10.1063/1.3607438)